Phase defect detection with spatial heterodyne interferometry

Philip R. Bingham[*a], Kenneth W. Tobin[a], Marylyn H. Bennett[b], and Pat Marmillion[b]
[a]Oak Ridge National Laboratory, PO Box 2008, Oak Ridge, TN 37831-6010
[b]International SEMATECH, 2706 Montopolis Drive, Austin, TX, 78741

ABSTRACT

Phase shift techniques introduced in photolithography to further improve resolution produce a new set of challenges for inspection. Unlike the high contrast provided by patterned and unpatterned areas on a binary mask, phase errors do not provide significant contrast changes, since the phase change is imparted by a difference in material thickness. Surface topology measurements can be used to identify phase defects, but methods for surface topology inspection are typically slow or can damage the surface to be measured. In this study, Spatial Heterodyne Interferometry (SHI) has been considered as a possible method for high-speed non-contact phase defect detection. SHI is an imaging technique developed at Oak Ridge National Laboratory that acquires both phase and amplitude information from an optical wavefront with a single high-speed image capture. Using a reflective SHI system, testing has been performed with a mask containing programmed phase defects of various sizes and depths. In this paper, we present an overview of the SHI measurement technique, discuss issues such as phase wrapping associated with using SHI for phase defect detection on photolithographic masks, and present phase defect detection results from die-to-die comparisons on a 248nm alternating aperture phase shift mask with intentional phase defects.

Keywords: Mask Inspection, Phase Defects, Spatial Heterodyne Interferometry

1. INTRODUCTION

Phase shift techniques introduced in photolithography to further improve resolution produce a new set of challenges for mask inspection systems. Due to the high contrast between the opaque pattern and substrate materials used for binary masks and the need to only detect defects in the pattern, inspection systems were able to locate binary mask defects by imaging the mask surface with a traditional intensity imaging system. Phase shifting techniques have produced another type of defect to be detected known as the phase shift defect. Phase shifting in masks is accomplished through two methods: etching the substrate material as in Alternating Aperture Phase Shift Masks (AAPSMs) and using a partially transmissive pattern material as in Attenuating Phase Shift Masks (AttPSMs)[1].

At Oak Ridge National Laboratory (ORNL), we have developed an imaging technique called Spatial Heterodyne Interferometry (SHI) that captures single images containing both phase and amplitude information at a high rate of speed. By measuring the phase of a wavefront reflected off of a surface, the relative surface heights can be determined. Since surface topology of a Phase Shift Mask (PSM) provides a measure of the phase shift differences between regions, SHI will allow detection of phase shift defects. The sensitivity of an SHI system for phase defects will depend on the wavelength in two ways. First, the spatial resolution is limited by the illumination wavelength of the inspection system. Secondly, the phase contrast for different defect depths will depend on the inspection wavelength.

A prototype imaging system built by ORNL for nLine Corporation to apply the SHI technology to high aspect ratio high-speed wafer inspection has been modified for photolithographic mask imaging [2]. The prototype tool known as the Visible Alpha Tool (VAT) captures the wavefront resulting from 532nm illumination reflecting off of the surface to be imaged. Testing has been performed on the VAT to begin to determine the sensitivity of SHI for phase defect detection on an AAPSM with programmed phase defects.

As background, the following subsections will describe SHI by explaining how it is performed and what is measured, discuss the phase shift structures used for resolution enhancement in optical lithography, and give a theoretical

[*] binghampr@ornl.gov; phone (865)574-5680

discussion on the application of SHI to phase defect inspection. Following the introduction, remaining sections detail the testing, results, and conclusions for phase defect detection experimentation performed with the VAT on an AAPSM with programmed phase defects.

1.1. Spatial heterodyne interferometry

Spatial Heterodyne Interferometry (SHI) is a technique that captures an interferogram which is then passed through a reconstruction algorithm that produces the phase and amplitude of the captured wavefront. Figure 1 shows a basic layout of a reflective SHI system. An illumination beam is emitted by the laser, which is then split into a reference arm path and a measurement arm path. The measurement arm path reflects the illumination beam off of the object to be imaged (in this case a photolithographic mask) while the reference beam is reflected off of a mirror to produce a flat reference image. The two wavefronts (measurement and reference) are then interfered on the surface of an imaging device (CCD Camera) with a small angle between the two beam paths. This small angle produces a spatial heterodyne frequency. Various lenses are used to provide the proper magnification and AOMs are used to allow shuttering and power balancing between the two arms.

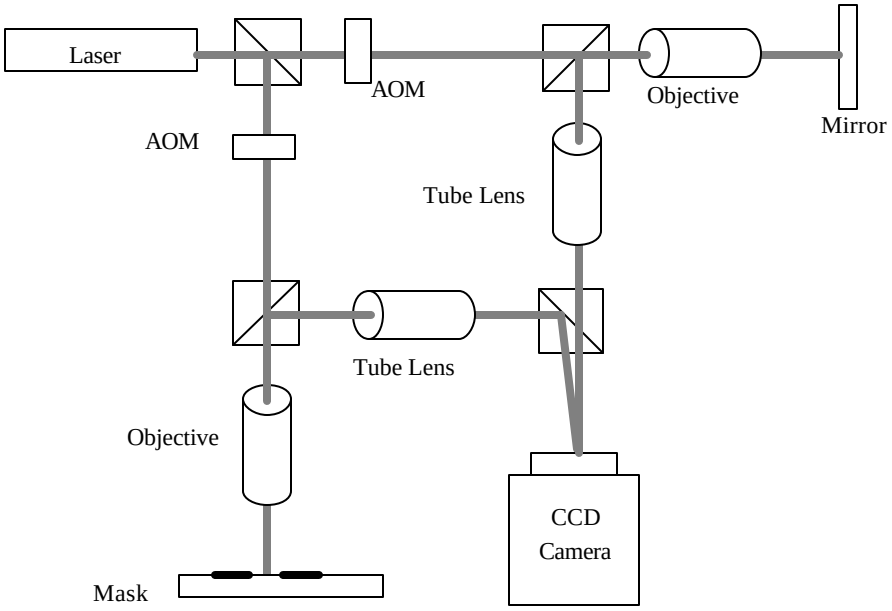

Figure 1. Basic layout for reflective spatial heterodyne interferometry.

Interfering the reference and measurement arms at a small angle introduces a phase wedge between the two beams. This phase wedge develops a linear fringe pattern across the image as seen in Figure 2. In order to show this mathematically, SHI image formation can be adequately described using scalar diffraction theory [3], where the reference wavefront ,$U_o(x,y)$, having amplitude, $A_0(x,y)$, and phase, $j(x,y)$, and the measurement wavefront, $U_M(x,y)$, having amplitude, $A_M(x,y)$, and phase, $y(x,y)$, are described as,

$$U_o(x,y) = A_o(x,y)\, e^{-jj(x,y)} \quad and \quad U_M(x,y) = A_M(x,y)\, e^{-jy(x,y)} \quad .$$

The intensity of the sum of these two wavefronts, $I(x,y)$, is recorded, e.g., on a photographic film media or in our case directly on the surface of a CCD camera, and is expressed as,

$$I(x,y) = \left|A_o(x,y)\right|^2 + \left|A_M(x,y)\right|^2 + 2\,A_o(x,y)\,A_M(x,y)\cos\left(y(x,y) - f(x,y)\right) \quad ,$$

which contains information not only regarding the intensity of the two waves, but also the relative phase between them at every spatial location (x,y). In SHI, the reference wavefront is considered to have uniform amplitude and phase over the entire wavefront. However, the two beams are interfered at an angle. In the mathematics, we can treat this angle as a wedge on the reference wavefront with slopes in the x and y directions proportional to w_x and w_y such that

$f(x,y) = 2p(w_x x + w_y y).$ As a simplification, we will assume that the reference amplitude is equal to 1 and baseline reference phase is 0° resulting in

$$I(x,y) = 1 + \left|A_M(x,y)\right|^2 + 2A_M(x,y)\cos\left[2p\left(w_x x + w_y y\right) - y(x,y)\right].$$

The frequency constants, (w_x, w_y), represent the spatial heterodyne frequency of the system. With this in mind, the diagonal fringes shown in Figure 2 represent the spatial carrier frequency (w_x, w_y) and fluctuations in the fringe intensity and position encode the amplitude and phase of the measurement wavefront respectively. Fourier frequency analysis is then used to isolate the carrier frequency information from the autocorrelation and reconstruct the phase and amplitude of the measurement wavefront [4]. Figure 3 shows the frequency domain image resulting from a Fourier transformation of Figure 2a showing the separability of the image on the carrier frequency from the autocorrelation image in the center.

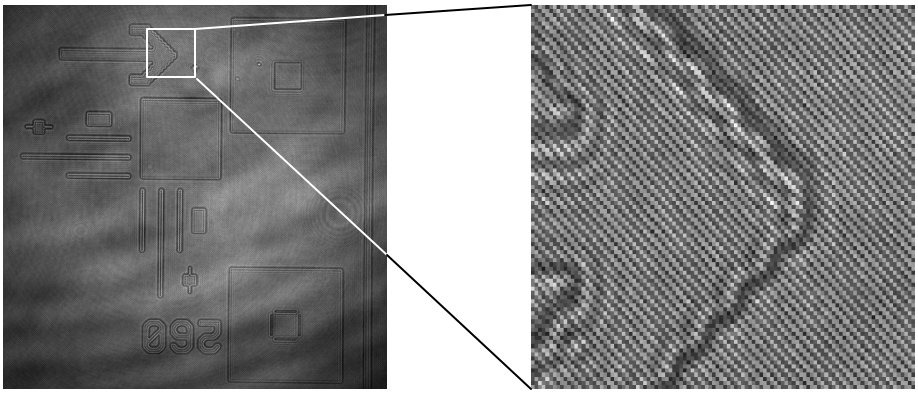

(a) **(b)**

Figure 2. SHI image (a) full image (b) magnified subsection showing diagonal fringe pattern.

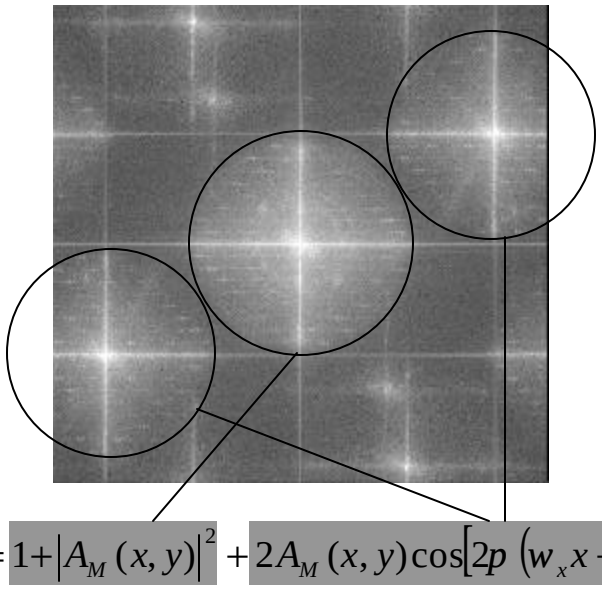

Figure 3. Frequency domain image showing separability of autocorrelation and carrier.

The result of the Fourier frequency analysis is the approximate determination of the original complex wavefront, i.e.,

$$U_F(x,y) = 2A_M(x,y)e^{-jy(x,y)} \approx U_M(x,y)$$

Once an estimate of the original complex wavefront, $U_F(x,y)$, has been determined, the amplitude and phase are determined by,

$$A_M(x,y) = \sqrt{\mathrm{Re}\{U_F(x,y)\}^2 + \mathrm{Im}\{U_F(x,y)\}^2} \quad \textit{and} \quad y(x,y) = \tan^{-1}\left(\frac{\mathrm{Re}\{U_F(x,y)\}}{\mathrm{Im}\{U_F(x,y)\}}\right),$$

where Re{} and Im{} represent the real and imaginary components of $U_F(x,y)$ respectively. Figure 4 shows the resultant phase of the chrome-on-chrome target imaged by the SHI image shown in Figure 2.

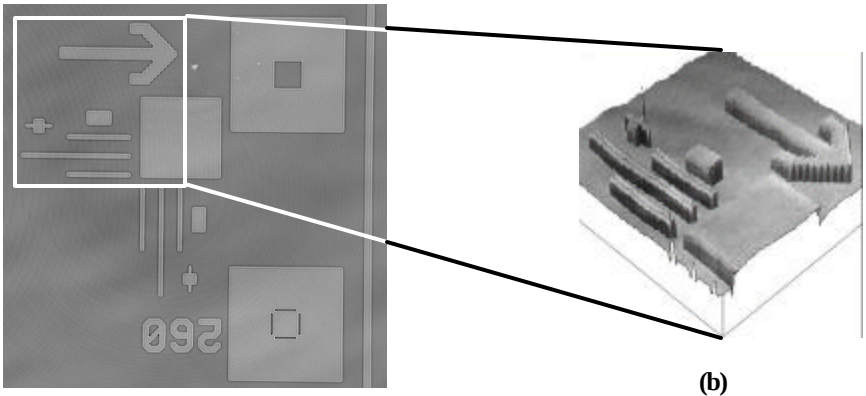

(a) **(b)**

Figure 4. Phase image reconstructed from a single SHI image. (a) phase image (b) 3-D representation of phase image.

1.2. Phase defect detection with SHI

As mentioned earlier, phase shifting techniques are being incorporated into photolithographic masks to further reduce the critical dimension that can be obtained with a particular illumination wavelength. Two phase shifting mask types have emerged, Alternating Aperture Phase Shift Masks (AAPSMs) and Attenuating Phase Shift Masks (AttPSMs). An AAPSM is similar to the common binary mask in that it consists of a substrate material such as quartz and an opaque pattern material (chromium). In AAPSM, the quartz is etched to produce phase shifts that differ in phase on either side of a pattern structure/line by 180 degrees. The two different phase illumination levels reduce ringing caused by diffraction at the pattern edges thereby creating a narrower printed line on the wafer than is possible without the use of phase shifting. The AttPSMs use the same concept to improve resolution, but do so by using a partially transmissive material for the pattern region. The transmissive material imparts a phase shift between light transmitted through the shifting material and the substrate material. The phase shift is determined by the thickness and index of refraction for the pattern material.

In both AAPSMs and AttPSMs, the phase shift imparted on the illumination beam is a function of the material's thickness and index of refraction. One way to directly measure the phase shift is by measuring the phase of a beam passing through the mask [5]. Another more indirect method is to measure the surface topology of the mask [6] and calculate the phase shift based on the known material indices of refraction. For defect detection, we are less interested in whether a method makes a direct measurement of the phase shift than we are in whether the phase defect produces a strong signal that can be detected. Obviously, the phase shift produces some change in the intensity of the image projected by the mask, so an aerial imaging system (AIMS) can be used to measure phase defects [7]. However, a direct AIMS image would likely be very insensitive to phase height errors. Common tricks to make phase information

more visible in the intensity image such as differencing between focus levels [1] can improve AIMS phase defect detection capabilities. However, we feel that SHI can further improve the visibility of phase defects.

Since SHI is a phase measurement tool, the first notion is to measure the transmitted phase to perform defect detection as is done in [5] where they are measuring the phase difference between two points on a mask. The SHI technique would allow phase measurement over large areas with millions of points per image capture enabling high-speed inspection. A transmission SHI system is currently under development. A reflective SHI measurement will also provide phase shift information due to topology variations and can be used to perform phase defect detection. A prototype reflective SHI system was used in this study as described in the following section.

For an AAPSM, what is the sensitivity of SHI measurements to a change in mask phase shift? This is calculated fairly easily. First one must determine the substrate thickness difference needed to create the desired phase shift for the mask projection wavelength. The etch depth is calculated as

$$d = \left(\frac{l_{Mask}}{i_S - i_{air}} \right) \left(\frac{\Delta q}{360^\circ} \right)$$

where l_{Mask} is the PSM illumination wavelength, i_S is the substrate index of refraction, i_{Air} is the index of refraction for air, and Δq is the desired phase shift. With the depth, we can calculate the phase for a reflected wavefront captured by SHI as

$$\Delta y = \mathrm{mod}\left(\frac{2d}{l_{SHI}}, 1 \right) * 360^\circ$$

where l_{SHI} is the SHI illumination wavelength. Finally, the transmission SHI phase response is given by

$$\Delta y = \mathrm{mod}\left(\frac{d(i_S - i_{Air})}{l_{SHI}}, 1 \right) * 360^\circ .$$

The mod functions in both the SHI responses are a result of wrapping in phase. Phase measurements can only have values from 0° to 360° thus phase measurements wrap from 360° back down to 0°. When performing reflective wavefront measurements or transmission wavefront measurements at the non-actinic wavelength, phase wrapping plays an important roll in the sensitivity of the phase defect detection.

The graph shown in Figure 5 was produced using the previous equations to show an example of reflective and transmissive SHI phase response at two wavelengths, 248nm and 532nm, versus phase defect height in degrees on an AAPSM designed for 248nm illumination. Many observations can be made from this graph. We will only point out a few. Beginning with the transmission response (dashed lines), the 248nm SHI response directly corresponds to the mask phase shift since it is at the designed wavelength. Using a longer wavelength will reduce the transmission SHI sensitivity as seen with the 532nm response line where a 180° phase error only produces a 90° phase response. In transmission SHI, no wrapping will occur over the designed mask phase shifts unless the SHI imaging wavelength is shorter than the actinic wavelength.

Since the phase shift imparted on a reflected wavefront is a result of path length differences instead of index of refraction differences, the reflected SHI responses will produce wraps for both the 248nm and 532nm reflective SHI responses. For the graphed example, the 248nm reflective SHI response will wrap at approximately every 90° of mask phase shift, and the 532nm reflective SHI will wrap at approximately every 195° of mask phase shift. While wrapping may be seen as bad since it makes certain phase shift errors difficult to detect. As shown in the graph, the reflective SHI response curves have a steeper slope over the first 90° the transmission SHI response curves. This steep slope means greater sensitivity for phase errors in this range. Therefore, if most phase errors are expected to be in this range, a reflective SHI system will provide more sensitive defect detection. For example, a 10° phase defect will produce a phase result of 18° for 532nm reflective and 39° for 248nm reflective where the transmission systems only produce 5° and 10° for 532nm and 248nm illumination respectively.

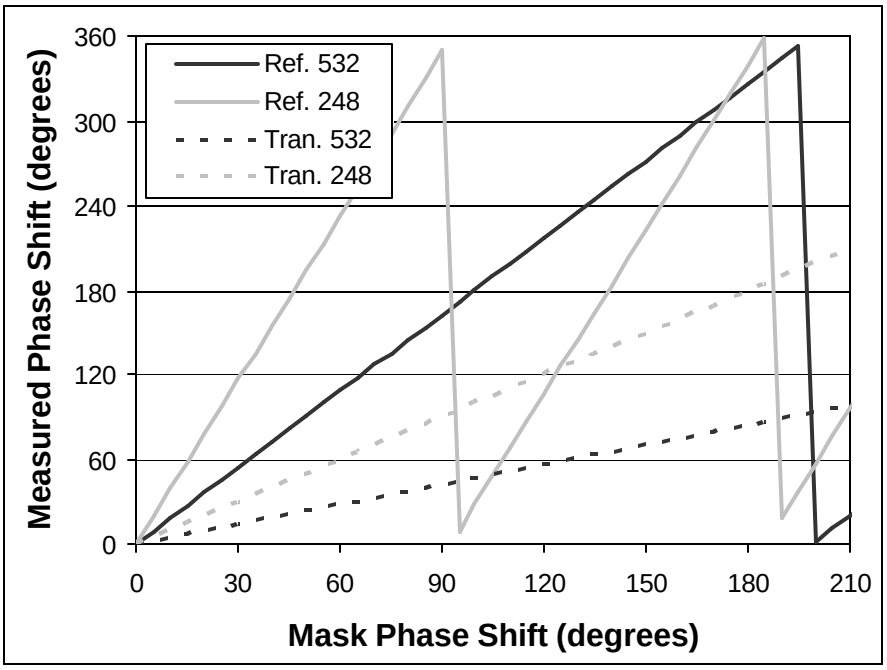

Figure 5. Phase measurements from reflection and transmission SHI with 532nm and 248nm illumination versus the phase shift for AAPSM with actinic wavelength of 248nm.

2. TESTING

A prototype imaging system built by ORNL for nLine Corporation to apply the SHI technology to high aspect ratio high-speed wafer inspection has been modified for photolithographic mask imaging [2]. This prototype tool known as the Visible Alpha Tool (VAT) captures the wavefront resulting from 532nm illumination reflecting off of the mask surface. While the VAT has been modified to hold masks, no modifications were made to the algorithms originally designed for defect detection on wafers. The VAT images/inspects with a field of view equal to 120μmx120μm on the mask. Ideally inspections could be performed at the CCD camera frame rate of 30 frames per second. In reality, the reconstruction algorithm limits the VAT to two frames per second. Since the VAT is a laboratory test system, we have not concentrated on accelerating the reconstruction. However, this is a highly parallel problem when capturing streams of images that can and has been accelerated with multiprocessor units on the nLine wafer inspection tools.

A DuPont Photomask AAPSM designed for 248nm was used in this study to test reflective SHI on phase defects. This mask contains a variety of programmed phase defects in an array that enables the die-to-die algorithms employed for wafer defect detection to be used. In this section we describe the mask used for testing and the tests performed to determine the capabilities of reflective SHI for phase defect detection on the test mask

2.1. Mask description

While the AAPSM mask contains several different test regions, the area used for phase defect detection testing consists of sets of lines in an alternating aperture setup with a line print size of 130nm. Figure 6 is a phase image from the VAT showing the pattern on the mask in which the phase defects are placed. In this image, the material around the edges and forming lines throughout is the pattern material. The phase shift regions on either side of each line can be seen as an alternating dark-light pattern indicating that the VAT is able to distinguish between the 0° and 180° phase shift regions use on an AAPSM. The mask is 4:1, so the pattern lines are 520nm wide. Spaces (quartz regions) between the lines are twice the line width or 1040nm. For each defect type and size, the pattern is printed multiple times to facilitate defect detection through die-to-die subtraction.

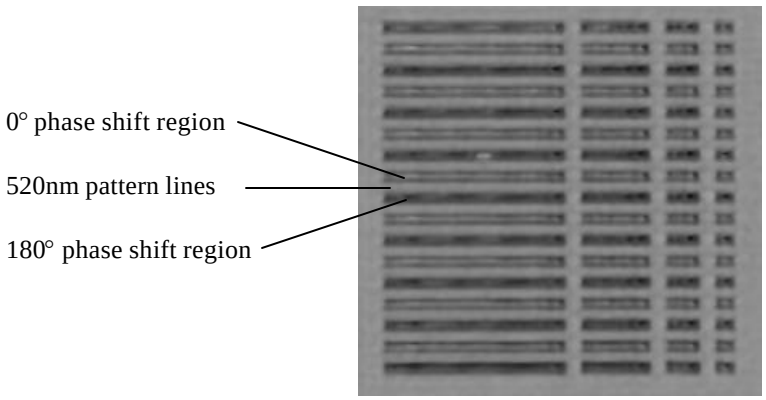

Figure 6. Mask pattern description.

The mask contains 18 different types of phase defects with sizes ranging from 50nm up to 500nm in 50nm steps. The 18 different types can be divided into three major subsets (2X wide edge, 1X wide edge, and corner). Within each subset the defect is produced at three phase heights (60°, 120°, and 180°) and as both bumps and divots. The graph in Figure 5 indicates that the VAT (532nm reflective SHI tool) should have good phase response for all three phase defect heights. 60° defects will produce a 110° phase response, 120° will produce -140°(220°) response, and 180° will produce a response of -30°(330°).

The first subset of defects is 2X wide edge defects. These defects are 2 times longer than they are wide such that the 50nm defect is 50nm x 100nm and the defects lie along the edge of a phase shift region far from a corner. Examples of this subset are shown in Figure 7 with an AFM scan over the defect. In these images, the highest area is the pattern material showing two lines with a phase shift region between. The divot is then etched out of the phase shift region to create the desired phase shift error. As expected, the divot gets deeper as the phase shift error increases. The second set of defects is 1x wide edge defects. These defects have equal height and width dimensions and are located along the edge of a phase shift region. The final subset consists of corner defects. The corner defects are located in the corner of a phase shift region and have equal height and width dimensions. AFM scans for three different corner defects are shown in Figure 8. As the defects in Figure 8 are bump type, the bump height increases with the phase shift value. Figure 9 shows the reconstructed phase of reflective SHI images taken by the VAT of the same defect types shown in Figure 7 and Figure 8 with the defect circled in the image. These results are very encouraging due to the high visibility of the defects.

From Figure 5 the VAT phase response for 60° phase defects on a 248nm mask is ≈110°; the response for a 120° phase defect is ≈220°; and the response for a 180° phase defect is ≈330°. With phase subtraction, results actually fall between +180° and -180° so the responses for 60°, 120°, and 180° phase defects are 110°, -140°, and -30° respectively. Thus, we expect all three phase defect depths on the mask to be quite visible on the VAT.

Figure 7. AFM scans of 2 x Wide Divots. (Images reproduced with permission from [8])

Corner bump 180° Corner bump 120° Corner bump 60°

Figure 8. AFM scans of corner bump defects.(Images reproduced with permission from [8])

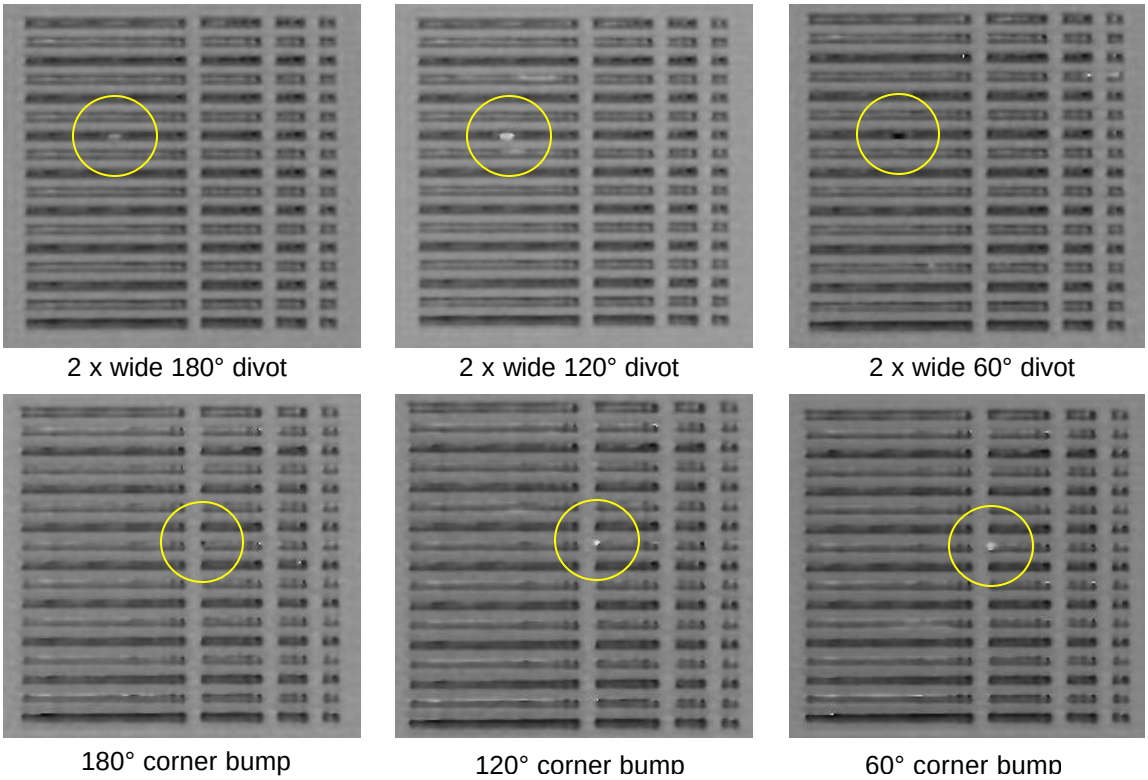

Figure 9. VAT phase images of quartz defects.

2.2. Test procedure

As mentioned previously, the VAT is a reflective SHI imaging system originally developed for defect detection on semiconductor wafers. Modifications made to the chuck allow masks to be imaged by the system, but no other modifications to the control and image processing (defect detection) software have been made. In order to use the system with no software modifications, a detection run was performed for each phase defect individually. Each run captured an image of the same position in three different die, reconstructed the phase and amplitude for each image, and performed detection by comparing the three complex images. Figure 10 gives an overview of the comparison between the three die with an example. The first column shows three of the actual phase images for a 2X wide edge divot with a depth causing 120° of phase shift and a size of 500nm x 1000nm. The second column shows the results of comparisons between neighboring die. This comparison is an algorithm that uses both the phase and amplitude of the images to acquire the shown difference images. The final column contains the defect mask for the center die and is the result of combining the two difference images in column 2 and thresholding to locate the 120° phase defect in the example.

Once the detection is complete, the defect masks were inspected by an operator to determine whether each defect was detected. In many cases, additional defects appeared requiring the operator to refer to the difference, phase, and amplitude images to determine whether the detections were false positives. Many of the non-programmed defects appear to be true defects, thus we were unable to provide performance with respect to false positives. However, in order to provide a conservative estimate of performance, thresholds were set to keep the number of non-programmed defects very low (no more than a couple extra defect per detection sequence) keeping in mind that many of the extra defects were real based on review of the phase and difference images. To put this in perspective, a detection sequence inspects a region 120μm^2 or about 10 times the area shown in the phase images of Figure 10 and each image contains 9 copies of the region shown in the phase images.

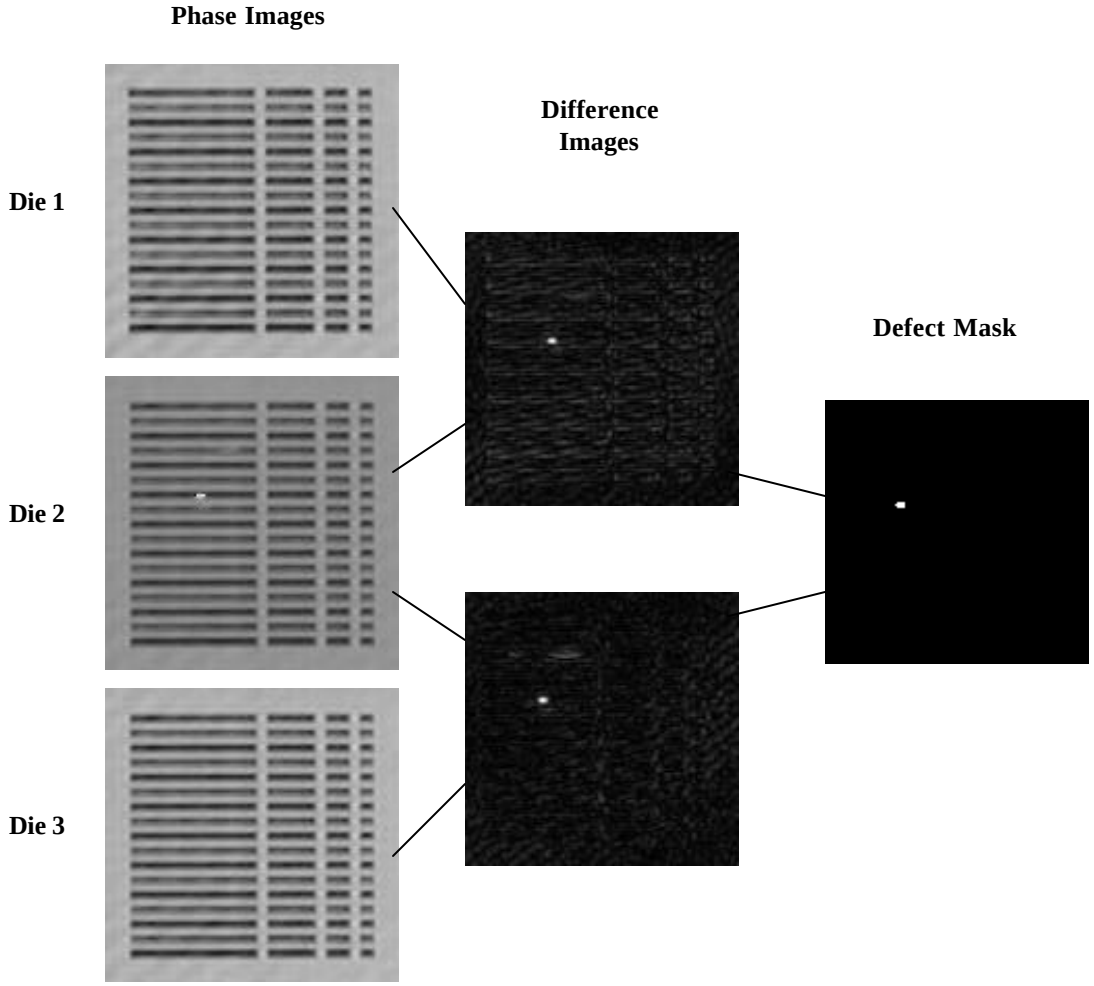

Figure 10. Die-to-die defect detection.

3. DEFECT DETECTION RESULTS

The detection sequence described in the previous section was performed on all sizes of each phase defect type present on the mask. Defects were labeled as detected if contained in the resulting defect mask and little or no extra defects were present. Unfortunately, we know that many of the extra defects we see are real defects and are therefore unable to make a comment on the number of false positives other than saying it was kept extremely low. The tabulated detection results are shown in Table 1. The dark gray areas of the table indicate that the defect was detected. The light gray areas indicate that the defect was visible in the difference images but did not pass the threshold. Based on previous experience with defect detection on wafers with SHI, we feel that these misses are likely caused by focusing errors.

Much effort has been placed in developing autofocus method for wafers on the VAT, but these algorithms are not directly applicable to masks and need modification to improve the focus capabilities for masks. As a result, a rudimentary autofocus was used for these tests assuming the mask to be a plane of constant slope; therefore, we are confident that most of the defects labeled in light gray on the table can be detected with improved focus algorithms.

These results show that the VAT was able to detect most of the defects one would expect due to the relatively long illumination wavelength (532nm). While we have gone into detail about the expected phase response, we have not mentioned the spatial resolution due to the illumination wavelength. For coherent illumination, the spatial resolution is approximately half the wavelength, so spatial resolution is approximately 266nm for the VAT. In the table, 79% of the defects 250nm and larger were detected. Most of the defects that were missed are corner bumps and 1x wide edge bumps. For the defect detection runs, off-axis illumination was used to reduce back reflection noise. One possibility is that the illumination angle essentially hid these defects behind neighboring pattern structures. In addition to performing well on defects within the resolution of the system, the VAT was also able to detect many of the defects below the illumination resolution (<250nm).

Table 1 - Detection results from the 532nm VAT on a 248nm DuPont AAPSM.

Size(nm)										
50	100	150	200	250	300	350	400	450	500	Quartz Defect Type
										2xWide Edge Divot 180°
										2xWide Edge Divot 120°
										2xWide Edge Divot 60°
										1xWide Edge Divot 180°
										1xWide Edge Divot 120°
										1xWide Edge Divot 60°
										Corner Divot 180°
										Corner Divot 120°
										Corner Divot 60°
										Corner Bump 180°
										Corner Bump 120°
										Corner Bump 60°
										2xWide Edge Bump 180°
										2xWide Edge Bump 120°
										2xWide Edge Bump 60°
										1xWide Edge Bump 180°
										1xWide Edge Bump 120°
										1xWide Edge Bump 60°

Not detected
Possibledetection with additional focus work on VAT
Detected with VAT

4. CONCLUSIONS

In conclusion, this study has shown that reflective SHI is capable of performing phase defect detection on AAPSMs. With the capability to measure phase of a reflected wavefront, SHI can see surface height differences in phase shift regions. However, as with any phase measurement, phase wrapping issues must be considered to determine if the inspection wavelength provides a strong phase signal for the phase defect heights to be detected. Using a shorter wavelength will increase the number of wraps, but will also increase the signal level for small phase defects making them more visible.

While other measurement techniques can produce surface topology images for phase defect detection, reflective SHI does so at a high rate of speed with a single image capture. The images captured for this work used exposures <1msec to capture a 1k x 1k image over a 120µm x 120µm region of the mask. The current camera on the VAT can capture 30 frames per second. Therefore, the limiting factor is reconstruction of the phase and amplitude images. The current PC

on the VAT can only sustain a 2 frames/second reconstruction rate, but this is a highly parallel problem when reconstructing a stream of images that can and has been accelerated with a multiprocessor system.

Further testing is needed to get a more precise measure of defect detection performance. This testing needs to address several issues such as repeatability, the effect of off-axis illumination on detection, and focus improvements. As a final comment, the defect detection results are very good for this type of test considering algorithms designed to perform defect detection for wafers were directly applied to masks, and the defect detection results will likely get better with improvements in the autofocus and defect detection algorithms that tailor these algorithms for masks.

ACKNOWLEDGEMENTS

We would like to thank nLine Corporation for use of the VAT and International SEMATECH for mask metrology funding that enable conversion of the VAT for mask imaging.

This paper was prepared by the OAK RIDGE NATIONAL LABORATORY, Oak Ridge, Tennessee, 37831-6285, operated by UT-BATTELLE, LLC for the U.S. DEPARTMENT OF ENERGY under contract DE-AC05-00OR22725.

REFERENCES

1. Wong A.K., Resolution Enhancement Techniques in Optical Lithography, SPIE Press, Bellingham, Washington, ISBN 0-8194-3995-9, Chapters 5-6, 2001.
2. Bingham, P.R., Tobin, K., Bennett, M.H., Marmillion, P., *Preliminary results for mask metrology using spatial heterodyne interferometry*, Proc. SPIE, Vol. 5256, pp. 1331-1342, 2003.
3. J.W. Goodman, Introduction to Fourier Optics, McGaw-Hill Physical and Quantum Electronics Series, McGraw-Hill Book Co., New York, New York, 1968.
4. E. Voelkl, L.F. Allard, D.C. Joy, Introduction to Electron Holography, Kluwer Acedemic Press / Plenum Publishers, New York, New York, 1999.
5. Jacob, J.J., Litvin, T., and Merriam, A.J., *High-Resolution Photomask Transmission and Phase Measurement Tool*, SPIE, Vol. 4689, pp. 70-82, 2002.
6. Miller, K., and Todd, B., *Automated atomic force metrology applications for alternating aperture phase shift masks*, SPIE, Vol. 4186, pp. 681-687, 2002.
7. Rosenbusch, A., Hemar, S., Kenan, B., *Inspecting alternating phase-shift masks by matching stepper conditions*, SPIE, Vol. 4889, pp. 247-252, 2002.
8. Chen, J.X., Riddick, J, Lamantia, M, Zerrade, A., Henderson, R.K., Hughes, G.P., Tabery, C.E., Phan, K.A., Spence, C.A., Winder, A.A., Stanton, W.A., Delarosa, E.A., Maltabes, J.G., Philbin, C.E., Litt, L.C., Vacca, A., Pomeroy, S., *ArF (193-nm) alternating aperture PSM quartz defect repair and printability for 100-nm node*, SPIE, Vol. 4562, pp. 786-797, 2002.